

Strain-induced changes of the electronic properties of *B*-site ordered double-perovskite Sr₂CoIrO₆ thin films

S. Esser,¹ C. F. Chang,² C.-Y. Kuo,² S. Merten,³ V. Roddatis,⁴ T. D. Ha,² A. Jesche,¹ V. Moshnyaga,³ H.-J. Lin,⁵ A. Tanaka,⁶ C. T. Chen,⁵ L. H. Tjeng,² and P. Gegenwart^{1,*}

¹*Experimentalphysik VI, Center for Electronic Correlations and Magnetism, Augsburg University, D-86159 Augsburg, Germany*

²*Max Planck Institut für Chemische Physik fester Stoffe, D-01187 Dresden, Germany*

³*I. Physikalisches Institut, Georg-August-Universität Göttingen, D-37077 Göttingen, Germany*

⁴*Institut für Materialphysik, Georg-August-Universität Göttingen, D-37077 Göttingen, Germany*

⁵*National Synchrotron Radiation Research Center, 101 Hsin-Ann Road, Hsinchu 30076, Taiwan*

⁶*Department of Quantum Matter, ADSM, Hiroshima University, Higashi-Hiroshima 739-8530, Japan*



(Received 12 January 2018; revised manuscript received 16 April 2018; published 15 May 2018)

B-site ordered thin films of double perovskite Sr₂CoIrO₆ were epitaxially grown by a metalorganic aerosol deposition technique on various substrates, actuating different strain states. X-ray diffraction, transmission electron microscopy, and polarized far-field Raman spectroscopy confirm the strained epitaxial growth on all used substrates. Polarization-dependent Co *L*_{2,3} x-ray absorption spectroscopy reveals a change of the magnetic easy axis of the antiferromagnetically ordered (high-spin) Co³⁺ sublattice within the strain series. By reversing the applied strain direction from tensile to compressive, the easy axis changes abruptly from in-plane to out-of-plane orientation. The low-temperature magnetoresistance changes its sign respectively and is described by a combination of weak antilocalization and anisotropic magnetoresistance effects.

DOI: [10.1103/PhysRevB.97.205121](https://doi.org/10.1103/PhysRevB.97.205121)

I. INTRODUCTION

Double perovskites (DPs) *A*₂*BB'*O₆ display interesting electronic and magnetic properties, strongly depending on the degree of the *B*-site ordering, which as well is determined both by size and valence mismatch of the involved *B*-site cations [1–3]. In addition, epitaxial stabilization in thin films could lead to an improvement of *B*-site ordering as observed, for example, in the La₂FeCrO₆ system [4]. The most prominent ordering type of the *B*-site cations is the rocksaltlike structure with alternating *B* and *B'* planes along the pseudocubic [111]_{pc} direction [1], shown in Fig. 1 for the title compound of this study. Aside from the ferrimagnetic half-metal Sr₂FeMoO₆ [5] there are other highly insulating ferromagnetic ordered DPs, such as multiferroic La₂CoMnO₆ [6] and Ba₂CuOsO₆ [7], a magnetic insulator recently synthesized under high pressure.

Recently, correlated oxides with strong spin-orbit (SO) coupling attracted great attention. In particular, the SO coupling in iridates with Ir⁴⁺ (*5d*⁵ configuration) ions in octahedral coordination results in four occupied $J_{\text{eff}} = \frac{3}{2}$ and two half-filled $J_{\text{eff}} = \frac{1}{2}$ states [8]. As was first verified for the layered perovskite Sr₂IrO₄ [9], already a moderate Coulomb repulsion is sufficient to induce a SO Mott insulating state, with magnetic $J_{\text{eff}} = \frac{1}{2}$ moments. SO coupling is also important for semimetallic iridates [10]. As realized by Jackeli and Khallulin [11], novel magnetic exchange interactions, in particular the honeycomb Kitaev exchange [12], can arise from $J_{\text{eff}} = \frac{1}{2}$

magnetic moments. This initiated strong interest in two- and three-dimensional honeycomb iridates [13].

Iridate DPs offer another novel playground to investigate the electronic and magnetic properties arising from the competition of SO coupling, electronic correlations, and structural distortions. This leads, for example, in Sr₂CeIrO₆ (cf. Fig. 1) to an insulating state with weak antiferromagnetic (AFM) orbital order [16]. Also, both La₂MgIrO₆ and La₂ZnIrO₆ host SO Mott insulating magnetic states [17]. Sr₂YIrO₆ represents a class of DPs with Ir⁵⁺ configuration and evidence of novel magnetism has been reported [18]. However, subsequent work [19], also on the isoelectronic Ba₂YIrO₆ [20] related these observations to diluted paramagnetic impurities.

Strontium-iridate derived DPs may also be interesting from the perspective of tuning the properties of the semimetallic three-dimensional perovskite SrIrO₃ to a topological state. A tight-binding model for this material in Ref. [21] revealed a symmetry-protected nodal line made of $J_{\text{eff}} = \frac{1}{2}$ bands below the Fermi level. The same work proposed that the line node can be lifted enabling strong topological insulator behavior if sublayer reflection symmetry could be broken and SrIrO₃-based *B*-site ordered DPs such as Sr₂CoIrO₆ (SCIO) were suggested as a possible route for realization.

There were very few reports [15,22] on the bulk SCIO, prepared as polycrystalline samples by solid-state reaction from mixtures of oxides and carbonates. SCIO crystallizes in the monoclinic structure with the space group *I*2/*m* and pseudocubic lattice constants *a* = 0.3909 nm, *b* = 0.3925 nm, and *c* = 0.3921 nm. The Co/Ir ordered structure is stabilized due to a large difference in cation radii between Co³⁺

*philipp.gegenwart@physik.uni-augsburg.de

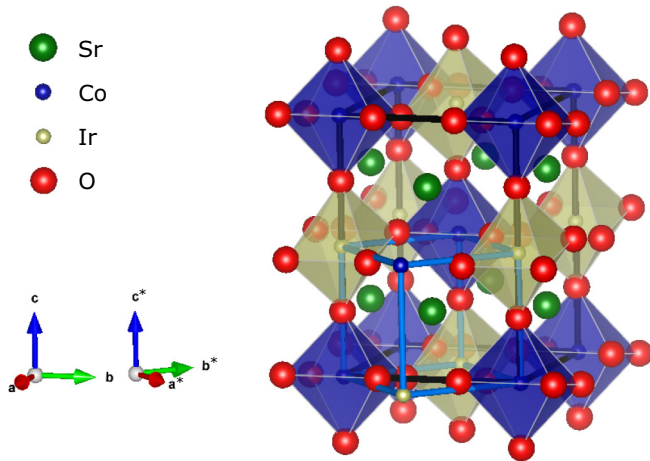


FIG. 1. Crystal structure of $\text{Sr}_2\text{CoIrO}_6$ (B -site mixing not shown) visualized with VESTA [14] based on Ref. [15]. The light blue cell indicates the pseudocubic (pc) unit with rocksalt-type ordering at the B sites. Note the superstructure with alternating Ir and Co layers along the $[111]_{\text{pc}}$ direction.

(0.061 nm) and Ir^{5+} (0.057 nm) ions. The antiferromagnetic (AFM) ordering with $T_N \sim 70$ K (AFM Curie-Weiss temperature $\Theta = -138$ K) and very small spontaneous magnetization $M \approx 0.005 \mu_B/\text{f.u.}$ was detected. The electron transport was found to be an insulatinglike scenario obeying a Mott variable-range hopping scenario with a gap ~ 0.05 eV.

Here, we report the growth, structure, and electronic properties of SCIO thin films, prepared by metalorganic aerosol deposition (MAD) technique, which employs an oxygen-rich growth atmosphere and enables to prepare high-quality perovskite thin films [23–25]. The Co^{3+} high-spin state and, consequently, the Ir^{5+} configuration was obtained, that is different as compared to the SrIrO_3 perovskite. Another motivating question was whether an incomplete B -site order with about 13.2% site mixing in previously reported bulk SCIO [22] could be improved by the in-plane epitaxial strain in thin films and how the electronic and magnetic properties will be influenced by epitaxial strain. Coherently strained SCIO thin films were epitaxially grown on various perovskite substrates and demonstrate a remarkable strain control of magnetotransport. By changing from tensile to compressive strain, a sign reversal of the magnetoresistance due to a change of the magnetic easy axis from in- to out-of-plane configuration was observed.

II. EXPERIMENT

Thin films of SCIO were grown by MAD on (111) oriented SrTiO_3 (STO), as well as on various pseudocubic (pc) (001) oriented substrates. The lattice mismatch of the used substrates ranges from -1.51% (GdScO_3) over -0.99% (DyScO_3), 0.05% (STO), and 0.96% (LSAT) to 1.09% (NdGaO_3), thus covering a broad range in both compressive and tensile direction. To protect the SCIO film, an STO capping layer was grown also by MAD directly after the SCIO film. Phase purity, crystal structure, and strain states were determined at room temperature by x-ray diffraction, using a PHILIPS

X'PERT diffractometer, operated with $\text{Cu-K}_{\alpha 1,2}$ radiation. The thickness of the films was determined from XRR measurements, performed by means of a BRUKER D8 ADVANCE diffractometer, and further simulated with the REMAGX [26] program.

The far-field Raman spectra were measured at room temperature by using a HORIBA Jobin Yvon LabRAM HR Evolution confocal Raman spectrometer in the back-scattering geometry. A neodymium-doped yttrium aluminum garnet laser with a wavelength of $\lambda = 532$ nm (second harmonic generation; Laser Quantum torus 532 with 100 mW, limited to 1 mW to avoid heating effects) is applied for excitation; the size of the laser spot was $\sim 1 \mu\text{m}$. For the polarization-dependent Raman measurements, the incident linear polarization of the laser can be tuned between P and S polarization by rotating a $\lambda/2$ wave plate. The scattered light polarization is determined by an analyzer with two switchable configurations (P polarization and S polarization) in front of the detector.

The high-resolution scanning transmission electron microscopy (HR-STEM) studies were carried out in a cross-section geometry using a FEI Titan 80-300 environmental transmission electron microscope operated at 300 kV and equipped with a Gatan Quantum 965ER image filter. The specimens were prepared using a focus ion-beam (FIB) machine (FEI Nova NanoLab 600 DualBeam instrument).

The polarization-dependent x-ray absorption spectroscopy (XAS) measurements were performed at the Dragon beamline of the National Synchrotron Radiation Research Center (NSRRC) in Taiwan. The spectra were recorded at 300 K using the total electron yield method (TEY) from SCIO films which were capped with 2-nm STO. The photon energy resolution at the $\text{Co } L_{2,3}$ edges was set at 0.3 eV and the degree of linear polarization was 99%. The samples were mounted on a holder which was tilted with respect to the incoming beam, such that the Poynting vector of the light makes an angle of 70° with respect to the $[001]_{\text{pc}}$ surface normal. By rotating the sample around this Poynting vector, the polarization of the electric field can be varied continuously from $E \parallel 20^\circ$ off the $[001]_{\text{pc}}$ surface normal, i.e., $E \parallel c$ (20°), to $E \perp$ the $[001]_{\text{pc}}$ surface normal, i.e., $E \parallel ab$. A CoO single crystal was measured simultaneously in a separate chamber to serve as an energy reference for $\text{Co } L_{2,3}$ edge.

The temperature and field dependencies of electrical resistance were measured by means of a Physical Property Measurement System (PPMS) using a four-probe van der Pauw geometry within external measurement setup due to the high resistance, $\sim \text{M}\Omega$, of films at low temperatures. The STO capped samples were microstructured for the resistance measurement by an *in situ* optical lithography without any contact to air between the subsequent steps. For this purpose, a special four-step method was developed, described in detail in the Supplemental Material (SM) [27].

The temperature- and magnetic-field-dependent magnetizations were measured in a 250-nm-thick SCIO film using a Magnetic Property Measurement System (MPMS) equipped with a 7-T magnet in a stabilized dc mode. For each measuring point, the raw background signal of the substrate was carefully subtracted from the measured raw signal of the sample and the resulting signal was analyzed in the standard way of the MPMS.

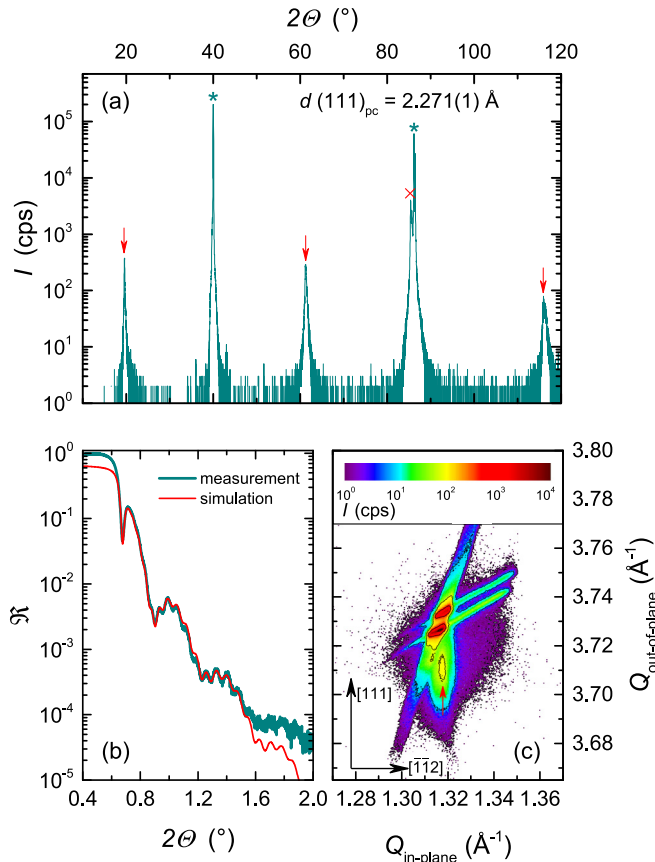


FIG. 2. (a) θ - 2θ XRD scan: Green stars indicating peaks from the (111)-STO substrate, the red cross shows the (222)-SCIO reflection and the arrows mark peaks due to ordered superstructure. (b) XRR measurement of an 84-nm-thick SCIO film with 21-nm STO capping including simulation with REMAGX [26]. (c) Reciprocal space map around the (112) peak of STO indicates fully strained thin film (arrow marks SCIO signal). The double-peak feature of STO substrate is owed by the Cu- $K_{\alpha 1}/K_{\alpha 2}$ doublet.

III. RESULTS AND DISCUSSION

A. Structural investigation

XRD measurements on $(111)_{pc}$ oriented thin films on $(111)_c$ STO [see Fig. 2(a)] indicate an out-of-plane epitaxy. The presence of B -site ordering in films was evidenced by observation of high-intensity $(\frac{1}{2} \frac{1}{2} \frac{1}{2})$ superstructure reflections, marked by red arrows in Fig. 2(a). The extracted pseudocubic out-of-plane lattice parameter $d(111)_{pc} = 2.271(1) \text{ \AA}$ for all studied SCIO/STO films with $d < 250 \text{ nm}$ is slightly larger than that measured for bulk SCIO, $d(111)_{pc} = 2.256 \text{ \AA}$ [15]. The reason is the in-plane compressive strain $\sim +0.05\%$ due to the lattice mismatch between SCIO and STO. Reciprocal space mapping around the (112)-STO peak [see Fig. 2(c)] confirms the fully strained state of the film. Small-angle XRR measurements in Fig. 2(b) indicate a large-scale homogeneity of all SCIO films, $d(\text{SCIO}) = 2\text{--}250 \text{ nm}$, as well as for the STO capping layer $d(\text{STO}) = 0\text{--}20 \text{ nm}$. The XRR signal can be well simulated with REMAGX [26] yielding extracted interface roughness of less than 2 nm.

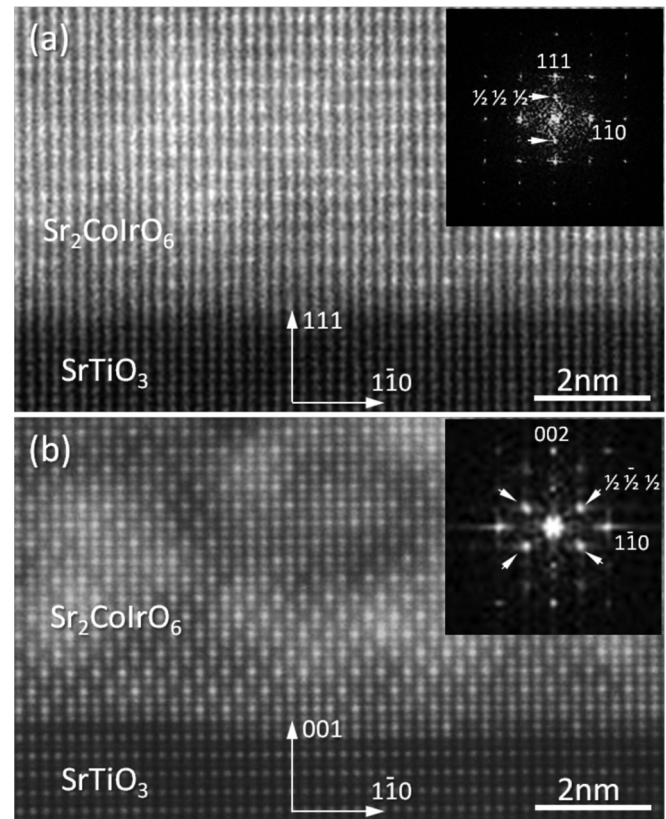


FIG. 3. HAADF HR-STEM images of the interface between SCIO grown on (111) (a) and (001) (b) STO substrate. Both images evidence a fully strained thin film with no defects at the interface. Fourier transformations of the SCIO film (insets) prove the (pseudo)cubic structure with ordered superstructure, indicated by additional $(\frac{1}{2} \frac{1}{2} \frac{1}{2})_{pc}$ spots.

HR-STEM images and corresponding FFTs in Fig. 3 confirm a high structural quality and the B -site ordering of SCIO films grown on (111) and (001) STO substrates. One can clearly see the pseudocubic symmetry with extra spots (white arrowheads) along the $[111]_{pc}$ direction due to the established B -site ordered superstructure. The SCIO/STO interfaces look coherent in agreement with results from the reciprocal space map, thus, evidencing a fully strained state of the film. Moreover, no dislocations or other defects are observed. Also, the B -site ordering is clearly seen in Fig. 3(b) since the atomic number of Ir is much larger than the atomic number of Co. The degree of Co/Ir ordering is estimated using HR-STEM image simulation to be more than 65% (see SM Fig. S3) [27].

To realize a biaxial tensile strain along the $[100]_{pc}$ and the $[010]_{pc}$ directions, we used substrates of GdScO₃ (GSO, $a_{pc} = 3.967 \text{ \AA}$) and DyScO₃ (DSO, $a_{pc} = 3.946 \text{ \AA}$) in $(001)_{pc}$ orientation. To exert biaxial compressive strain the $(001)_{pc}$ oriented SrTiO₃ (STO, $a_c = 3.905 \text{ \AA}$), LSAT ($a_c = 3.870 \text{ \AA}$), and NdGaO₃ (NGO, $a_{pc} = 3.865 \text{ \AA}$) were used.

In the top panel of Fig. 4, the evaluated linear relation between the out-of-plane film lattice parameter $d_{out-of-plane}$ and the pseudocubic substrate lattice parameter $a_{pc}^{substrate}$ is shown for STO(20 nm)/SCIO(20 nm) films. Within the linear

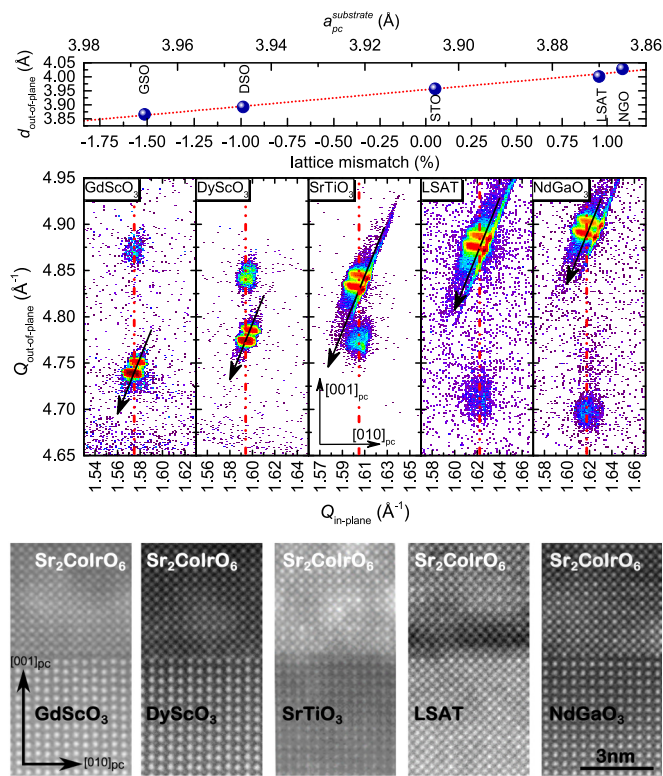


FIG. 4. Top panel: strain dependence of the out-of-plane lattice parameter, red line indicates linear behavior. Middle panel: reciprocal space maps around the (pseudo)cubic $(013)_{pc}$ peak of each used substrate indicating a fully strained thin film in each case. The double-peak feature for substrate (and in some cases also for the thin film) reflections is owed by the $Cu-K_{\alpha 1}/K_{\alpha 2}$ doublet. The black arrows always point towards the origin. The dashed red lines indicate the adaptation of the in-plane lattice parameter due to a constant in-plane scattering vector component. Bottom panel: HAADF STEM images of the SCIO-substrate interface for various substrates.

elasticity theory, this behavior indicates a fully strained state of films with the Poisson's ratio of $\nu = 0.407(8)$. Reciprocal space mapping around each (pseudo)cubic $(013)_{pc}$ substrate peak [see Fig. 4 (middle panel)] proves the fully strained state of each film grown on the used substrates. In addition, HAADF STEM images also verify the strained film/substrate $(001)_{pc}$ interfaces [see Fig. 4 (bottom panel)], preserved up to thickness ~ 50 nm of SCIO film.

In the case of STO as substrate material the B -site ordering was investigated by a $\theta-2\theta$ XRD scan in tilted geometry with \vec{Q} parallel to $\langle 111 \rangle_c$ of STO and, therefore, regarding the small lattice mismatch between SCIO and STO, also nearly parallel to $\langle 111 \rangle_{pc}$ of SCIO. The visible superstructure peaks in the collected XRD pattern [see Fig. 5(a)] could be well distinguished from the STO background, comparable to the results of the $(111)_{pc}$ oriented thin films [see Fig. 2(a)], and indicating well-developed B -site ordering. A larger lattice mismatch and therefore bigger difference between the $(111)_{pc}$ directions of substrate materials compared to strained SCIO, in combination with peaks appearing already from the bare substrate material at the crucial 2θ positions, is a key reason why this access is denied in case of the other used substrate materials.

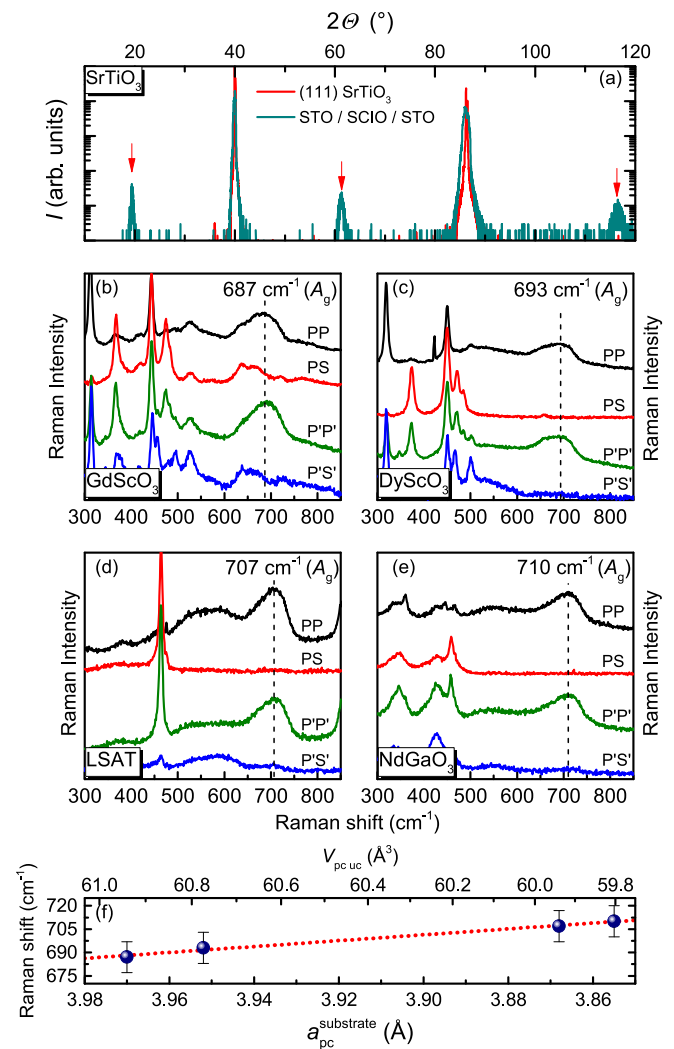


FIG. 5. (a) $\theta-2\theta$ XRD scan in tilted geometry with \vec{Q} parallel to $\langle 111 \rangle_c$ of STO: the arrows mark peaks due to the ordered superstructure. Polarized far-field Raman spectra of SCIO films on (b) GSO, (c) DSO, (d) LSAT, and (e) NGO at room temperature. The spectra are taken in the parallel PP ($P'P'$) and the crossed scattering PS ($P'S'$) configurations (with an additional in-plane rotation of $\Phi = 45^\circ$ around the $[001]_{pc}$ direction). (f) Strain dependence of Raman shift of the breathing mode; line indicates fully strained state with linear dependence.

To clarify the B -site ordering state in such SCIO films, we performed the polarization-dependent Raman spectroscopy [Figs. 5(b)–5(e)] and compare the data with other ordered double perovskites of the same point group, e.g., La_2CoMnO_6 (LCMO). B -site ordered LCMO obeys a monoclinic $P12_1/n1$ structure, for which theoretical lattice dynamical calculations [28] predict A_g stretching mode of the $(Co/Mn)O_6$ octahedra (breathing mode) at ~ 697 cm^{-1} . In contrast, the disordered LCMO obeys an orthorhombic $Pbmm$ structure and possesses the B_{1g} breathing mode. Similarly, we expect a $(Co/Ir)O_6$ breathing mode with A_g symmetry at a Raman shift, $RS \sim 697$ cm^{-1} , for the B -site ordered SCIO. In this case, the A_g mode should be present in Raman spectra, measured in parallel PP and $P'P'$ configurations, and it is forbidden

in the crossed scattering PS and $P'S'$ configurations [28–30] (the prime indicates measurements with an in-plane rotation of the sample by 45° around the $[001]_{pc}$ direction and provides an additional tool to test the epitaxy). For the disordered orthorhombic structure, the selection rules are opposite [28–30]. As one can see in Figs. 5(b)–5(e), all films in our strain series exhibit a strong breathing mode at $\sim 697\text{ cm}^{-1}$ in the parallel PP - and $P'P'$ -scattering configurations and only a weak (or none) intensity in the crossed PS and $P'S'$ configurations. Thus, the A_g symmetry and the B -site ordering can be concluded for all strained films grown on GSO, DSO, LSAT, and NGO. Furthermore, the Raman shift of the breathing mode [see Fig. 5(f)] was found to depend linearly on the strain $RS \sim -a_{pc}^{substrate}$. This is due to the change of the unit-cell volume $V_{pc\ uc}$, and of the phonon energy with strain. Note that a smaller $V_{pc\ uc}$ leads to a closer packing and, respectively, more energy is necessary. Kumar and Kaur [31] observed a similar behavior of the breathing mode in a strain relaxation series of the double perovskite $\text{La}_2\text{NiMnO}_6/\text{LaAlO}_3(001)$.

For selected films on GSO, STO, and NGO substrates, the B -site ordering was also studied on the microscale by HAADF STEM measurements along the $[110]_{pc}$ direction (see Supplemental Material [27]). These measurements show that independent of strain there are regions with a high degree of B -site ordering, which alternate with regions with lower or no B -site ordering at all. Concluding, the epitaxial strain perpendicular to the $[001]_{pc}$ direction could neither improve nor weaken the B -site ordering in SCIO.

B. Magnetic properties

Separation of magnetic properties of thin films from the substrate magnetic contribution is generally difficult. A comparison with data on bulk SCIO [22] indicates that a film with minimal thickness of $\sim 200\text{ nm}$ is required to get magnetic moment corresponding to $\sim 5\%$ of the moment of pure STO substrate at room temperature. Because fully strained $(001)_{pc}$ oriented SCIO films are stable for $d \leq 50\text{ nm}$, we focus here solely on thick ($d \sim 250\text{ nm}$) strained SCIO/STO $(111)_c$ films (cf. Fig. 1). However, we identified a $\text{Sr}_3\text{Co}_2\text{O}_6$ (SCO) second phase inclusion on the level 0.8 volume %. For a quantitative determination of the SCO volume fraction, we have used the field-dependent measurements of magnetization at lowest temperature (for more details, see Supplemental Material [27]). The foreign phase moments are saturated in a field of 7 T that has been applied in the measurement shown in Fig. 6. Furthermore, for our analysis of the difference between zero-field-cooled (ZFC) and field-cooled (FC) magnetization, it cancels out.

Previous investigation on polycrystalline SCIO revealed long-range magnetic order at 70 K, with ferromagnetic and antiferromagnetic components of the ordered magnetic moments, yielding to a pronounced difference in the FC and ZFC magnetization [22]. Figure 6 compares these literature data on polycrystalline SCIO (from Ref. [22], indicated by triangles) with the FC and ZFC magnetization measurements of our thick $(111)_c$ oriented SCIO film below 150 K. Compared to the polycrystal data, much weaker splitting between FC and ZFC is found and the maximum at 70 K in ZFC mode is absent. Taking the onset of the difference ΔM between FC

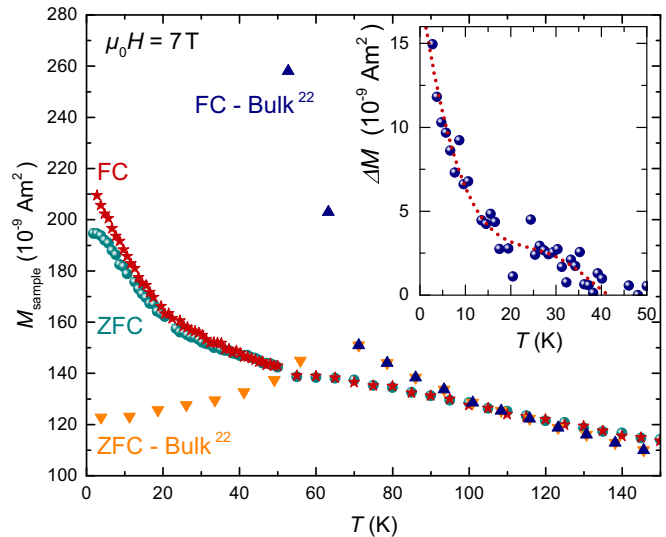


FIG. 6. Temperature dependence of FC and ZFC magnetization of $\sim 250\text{ nm}$ thick $(111)_{pc}$ oriented SCIO (after subtraction of the substrate background contribution) in comparison to literature data of bulk polycrystalline SCIO from [22] (scaled to the sample volume). Inset: temperature dependence of the difference between the FC and ZFC data (dotted line intended to guide the eyes).

and ZFC (see inset of Fig. 6) as measure of magnetic order, an ordering temperature of 43 K would be estimated for the film, which is significantly reduced compared to the polycrystal. We speculate that epitaxial strain and/or better B -site order is responsible for the difference in the magnetic susceptibility behavior.

In strained $(111)_{pc}$ oriented thin films of the double perovskite $\text{Sr}_2\text{FeMoO}_6$, Hauser *et al.* found a similar decrease of the ordering temperature [32]. Unfortunately, the thinner films of the $(001)_{pc}$ strain series could not be investigated by respective magnetization measurements and the evolution of the susceptibility behavior with strain remains therefore unknown.

C. Spectroscopic results

As mentioned in the previous section, the magnetic signal for the samples of the $(001)_{pc}$ strain series is too weak to be detected in a conventional SQUID magnetometer. In order to investigate the electronic structure and its antiferromagnetic property of the SCIO thin films, we resort to polarization-dependent XAS. Optical measurements were done on the SCIO films capped by 2-nm-thick STO [33], which due to its high integrity and insulating properties [34] protects SCIO films from degradation but still allows electrons to escape. We note that the polarization-dependent XAS is one of few techniques that can determine the magnetic axis of an antiferromagnetic ordered state in thin films [35–37]. Figures 7(a) and 7(b) show the experimental polarization-dependent Co $L_{2,3}$ XAS spectra of the most tensile strained SCIO thin films on GSO and the most compressive strained SCIO films on NGO, respectively, in this study, taken at 300 K. The spectra of the SCIO thin films on DSO, STO, and LSAT substrates are shown in Fig. S9 of the SM [27]. The spectra are dominated by the Co

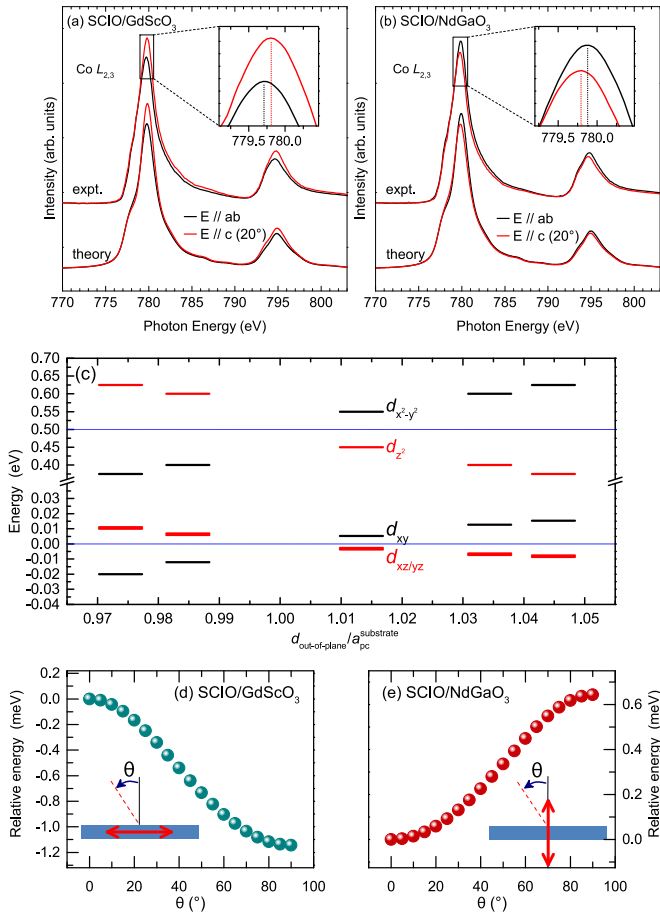


FIG. 7. Experimental polarization-dependent Co $L_{2,3}$ XAS spectra of (a) the most tensile strained SCIO films on GSO, and (b) the most compressive strained SCIO films on NGO in this study, taken at 300 K, together with the theoretical spectra calculated for Co^{3+} high-spin (HS) state. The inset of (a) and (b) is a zoom-in view at the L_3 main peak showing the favorite orbital state under different strains. (c) The energy level diagram of the orbital states of Co^{3+} in the SCIO films as a function of strain, obtained from the configuration interaction cluster model including the full atomic multiplet theory, which are consistent with the experimental polarization-dependent XAS results. (d), (e) The calculated magnetic anisotropy energy as a function of the spin direction of the SCIO films on GSO and NGO substrates, respectively. Each inset depicts a schematic drawing of the resulting AFM axis.

$2p$ core-hole spin-orbit coupling which splits the spectrum roughly in two parts, namely, the L_3 ($h\nu \approx 776\text{--}784$ eV) and L_2 ($h\nu \approx 793\text{--}797$ eV) white lines regions. The line shape strongly depends on the multiplet structure given by the Co $3d\text{--}3d$ and $2p\text{--}3d$ Coulomb and exchange interactions, as well as by the local crystal fields and the hybridization with the O $2p$ ligands. Unique to soft XAS is that the dipole selection rules are very sensitive in determining which of the $2p^5 3d^{n+1}$ final states can be reached and with what intensity, starting from a particular $2p^6 3d^n$ initial state ($n = 6$ for Co^{3+}) [38–40]. This makes the technique extremely sensitive to the symmetry of the initial state, i.e., the spin, orbital, and valence states of the ions.

The experimental XAS spectra show that the Co valence state of these SCIO thin films is mainly $3+$. Please note that

for comparing with the calculated spectra the experimental spectra in Figs. 7(a) and 7(b) have been subtracted by 10% and 8% of Co^{2+} , respectively. The experimental isotropic XAS spectra before subtracting Co^{2+} contributions can be found in Fig. S8 of the SM [27]. Further, the spectral features indicate a high-spin (HS) state of the Co^{3+} ions [38–40] in the SCIO thin films which is independent of substrates underneath, i.e., a strain-independent HS state. On the other hand, the orbital state in these SCIO thin films is quite different as indicated by the opposite sign of the polarization-dependent difference of spectra [35,36]. For example, the intensity of the L_3 main peak is always larger for $E \parallel c$ (20°) than for $E \parallel ab$ in the SCIO/GSO thin film, whereas it is always smaller in the SCIO/NGO thin film. Since these spectra were taken at 300 K, which is much higher than the magnetic ordering temperature of 43 K, the polarization contrast is caused solely by crystal-field effects. Using the E vector of light parallel to the ab plane (black lines), we can reach the unoccupied Co $3d$ orbital states with $xy/x^2\text{--}y^2$ characters. With the E vector of light parallel to the c axis (red lines), we detect the unoccupied Co $3d$ orbital states with $yz/zx/3z^2\text{--}r^2$ characters. This indicates that the sign of the crystal-field splitting is opposite in the two systems. This inference is further consolidated by the observed peak energy difference of the L_3 main line as depicted in the insets of Figs. 7(a) and 7(b). The L_3 peak position is higher for $E \parallel c$ (20°) than for $E \parallel ab$ in the SCIO/GSO thin film, while it is lower in the SCIO/NGO thin film. All together, we derive that in the tensile strained SCIO/GSO thin films the orbital states with x/y character are energetically favorable, whereas in the compressive strained SCIO/NGO thin films the orbital states with z character are energetically favorable. This can be understood qualitatively as the applied strain from the substrates underneath induces a tetragonal distortion and causes the corresponding orbital state shift in energy.

For further confirming this orbital energy level diagram and knowing the corresponding magnetic anisotropy, we have simulated the XAS spectra using the well-proven configuration interaction cluster model that includes the full atomic multiplet theory [41,42]. The calculations were performed using the XTLS 8.3 program [42]. For the calculation details, please see the SM [27]. As displayed in the bottom of Figs. 7(a) and 7(b), the calculated spectra based on the HS Co^{3+} model with the energy diagram of the orbital state shown in Fig. 9(c) can well reproduce the experimental spectra. We can safely conclude that a tensile strain stabilizes a ($3d^5 \uparrow\uparrow\uparrow\uparrow + 3d_{xy} \downarrow$) state and a compressive strain stabilizes a ($3d^5 \uparrow\uparrow\uparrow\uparrow + 3d_{yz/zx} \downarrow$) state in SCIO thin films. We infer that the change of the anisotropy in the crystal-field parameters in going from room temperature to low temperatures due to thermal contraction of the substrates is negligible, and that we therefore can use these XAS derived parameters also for the analysis of the low-temperature magnetic properties (see the Supplemental Material [27] for details). Accordingly, we can calculate the magnetic anisotropy energy as a function of the spin direction for each case as shown in Figs. 7(d) (tensile, SCIO/GSO) and 7(e) (compressive, SCIO/NGO). The magnitude of the exchange field was set to 4 meV in accordance with the magnetic ordering temperature of 43 K [40]. This magnetic anisotropy energy is expressed as $E = K_0 + K_1 \sin^2(\theta) + K_2 \sin^4(\theta) + K_3 \sin^4(\theta) \sin^2(\varphi) \cos^2(\varphi)$, where θ is the angle

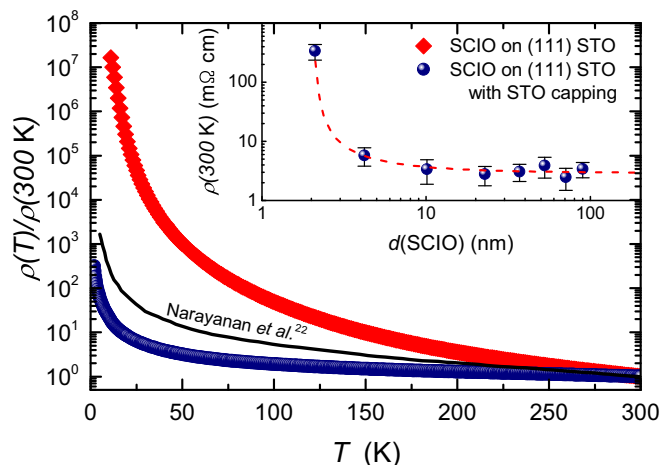


FIG. 8. Temperature dependence of the electrical resistivity of SCIO for a sample with STO protection (blue) and without protection (red) in comparison to bulk data (black line) obtained by Narayanan *et al.* [22]. Inset: thickness dependence of specific resistance at 300 K (dashed line as guide for eyes).

between the exchange field and $[001]_{pc}$, and φ is the azimuthal angle which is set to 45° . We find for the SCIO/GSO (tensile) $K_1 = -1.42$ meV, $K_2 = 0.14$ meV, and $K_3 = 0.56$ meV, while for the SCIO/NGO (compressive) we obtain $K_1 = 0.48$ meV, $K_2 = 0.08$ meV, and $K_3 = 0.33$ meV. In other words, for the tensile strained SCIO/GSO thin film, the spin moment favors the in-plane direction with the energy difference of about 1.14 meV between the magnetic easy axis ($\theta = 90^\circ$, in the film plane) and hard axis ($\theta = 0^\circ$, perpendicular to the film), whereas for the compressive strained SCIO/NGO thin film, the spin moment favors the out-of-plane direction with the energy difference of about 0.64 meV between the magnetic easy axis ($\theta = 0^\circ$, perpendicular to the film) and hard axis ($\theta = 90^\circ$, in the film plane). Note that the evaluated strain-induced AFM magnetic anisotropy in SCIO films, i.e., in/out of plane for tensile/compressive stress, differs from that observed for ferromagnetic double-perovskite films of $\text{La}_2\text{CoMnO}_6$, i.e., in/out of plane for compressive/tensile stress [43,44]. The reason is unclear up to now and, likely, is related to the FM exchange interaction between Co^{2+} and Mn^{4+} ions according to the second Goodenough-Kanamori-Anderson rule. This is a piece of useful information for understanding the magnetotransport properties of the SCIO thin films under different strains (see the discussion in the Sec. III E).

D. Zero-field transport properties

We now turn to the electrical resistivity of SCIO thin films. The temperature-dependent $\rho(T)$ measurements for a $(111)_{pc}$ oriented $d(\text{SCIO}) = 30$ nm thick SCIO film (with and without STO protective top layer) are shown in Fig. 8. Similar to the bulk SCIO (Ref. [22]), thin films also show an insulating behavior. The values of room-temperature resistivity for the air-protected and unprotected films were $3.08(1)$ m Ω cm and $6.66(1)$ m Ω cm, respectively. The reported bulk value (Ref. [22]) was about 3 and 1.5 times larger, respectively. Upon cooling to 4 K, the electrical resistance of the unprotected film strongly increases, becoming several orders of magnitude

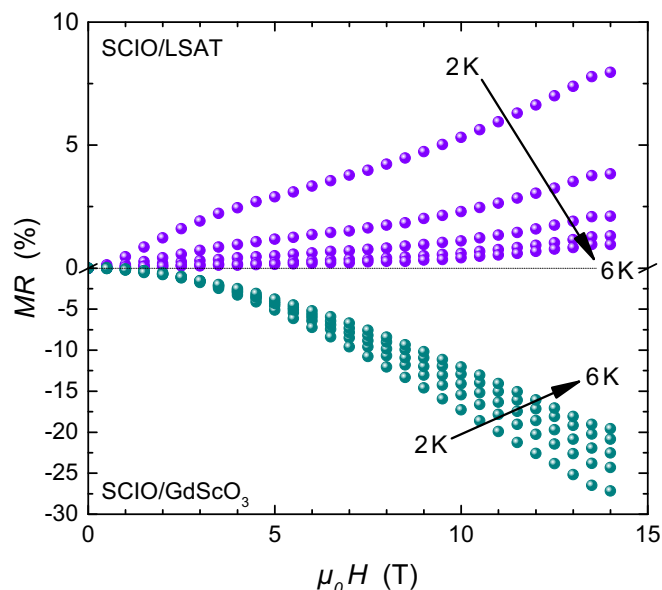


FIG. 9. Isothermal transverse magnetoresistance $\text{MR} = [\rho(H) - \rho(0)]/\rho(0)$ of $(001)_{pc}$ strained SCIO thin films grown on LSAT (compressive strain) and GdScO_3 (tensile strain) at various temperatures between 2 and 6 K (fields always applied transverse to the film planes).

larger than the resistance of the protected film; the $\rho(T)$ of the bulk SCIO lies in-between. This indicates the importance of the STO capping layer to protect the (surface) properties of SCIO. As shown in the inset of Fig. 8, the room-temperature resistivity is almost independent on the film thickness for $d > 5$ –8 nm. Unfortunately, it was impossible to probe the thickness dependence at low temperatures. Fitting the $\rho(T)$ data of the capped SCIO thin film between 250 and 300 K results in a charge gap of $32(5)$ meV [27]. Below 70 K, $\rho(T)$ indicates variable range hopping behavior [27].

The electrical resistivity of the various films, strained along the $(001)_{pc}$ direction, is discussed in the Supplemental Material [27]. The overall insulating behavior does not change, although a systematic enhancement of $\rho(300$ K) with strain is observed [27].

E. Magnetotransport within the $(001)_{pc}$ strain series

Considering the information on the magnetic anisotropy, obtained in the Sec. III C, we can now address the magnetotransport properties of the SCIO thin films under different strains. Next, we focus on the low-temperature isothermal magnetoresistance (MR) of $(001)_{pc}$ strained SCIO thin films. As discussed previously in Sec. III C, the magnetic easy axis in this series changes from “in-plane” to “out-of-plane” as the strain changes from tensile to compressive. This change of the magnetic anisotropy has a direct influence on the magnetoresistance. As shown in Fig. 9, MR below 6 K is *positive* for thin films grown under compressive strain on LSAT substrate and *negative* for those under tensile strain on GSO substrate. This indicates a direct relation between MR sign and magnetic anisotropy. This is further corroborated by the comparison of the MR at 2 K of all strained SCIO thin films, which, as shown in Fig. 10, follow this trend. This observation suggests a strong

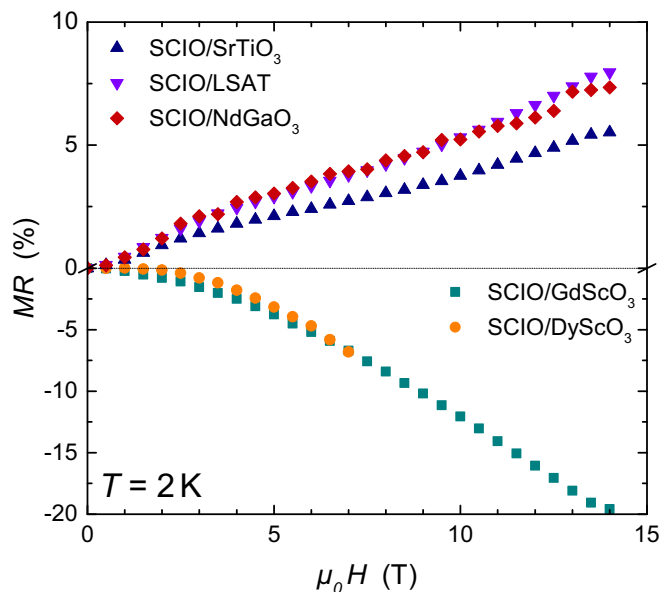


FIG. 10. Isothermal transverse magnetoresistance of all investigated $(001)_{pc}$ strained SCIO thin films at $T = 2$ K. Note that the thin film on DSO substrate broke in a field of $\mu_0 H = 7$ T due to a high magnetic torque effect from DSO.

influence of the anisotropic magnetoresistance (AMR) effect in combination with the reorientation of the AFM ordered Co sublattice in SCIO in an external transverse magnetic field.

In addition, structural disorder in combination with large spin-orbit coupling will generate a quantum correction to MR due to weak antilocalization (WAL). Based on the Dresselhaus effect [45] we used for the description of the WAL term of the MR a Dresselhaus-type contribution with isotropic spin-orbit scattering (see Supplemental Material [27]). For the AMR contribution, the orientation of the moments of Co sublattices in their AF ground state with respect to the field direction is important. For tensile strain at zero field the moments are oriented in the film plane and application of a transverse field leads to a continuous rotation of both sublattice moments out of the plane. This leads to a negative MR. For compressive strain, the moments of the two sublattices initially point parallel and antiparallel to the applied field. If there would be very weak coupling between the two sublattices, only the moments of the antiparallel sublattice would continuously rotate towards the applied field direction with increasing field. In the alternative case, upon increasing magnetic field, the moments remain in their orientation until a spin flip occurs (for a sketch, see Supplemental Material [27]), followed by continuous rotation towards the field. Since there is no indication for a sharp spin flip, we modeled the MR behavior in a smeared spin-flip scenario. For more details, we refer to Supplemental Material [27].

By combining AMR and WAL, a valuable quantitative description of the measured MR is possible for all strained SCIO thin films. This is exemplified in Fig. 11 for compressively strained SCIO. Within the smeared spin-flip scenario, a positive AMR contribution to the MR dominates between 10 and 24 T [27]. As detailed in the Supplemental Material, the obtained parameter for the WAL and AMR contributions

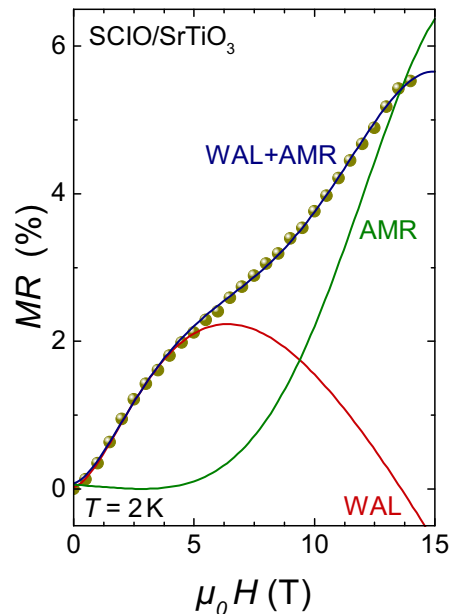


FIG. 11. Field dependence of the MR of SCIO on STO at $T = 2$ K. The red and green lines indicate the contributions of the WAL and AMR effects to the total signal. For the latter contribution, a smeared spin-flip scenario, detailed in the Supplemental Material [27], has been utilized.

within the smeared spin-flip scenario is more realistic compared to the assumption of very weak coupling between the two Co sublattices. To point out our key arguments, note the following: We expected a positive contribution from AMR and a temperature-independent spin-orbit scattering field within the WAL contribution. Both are only the case in the smeared spin-flip scenario.

As indicated by Fig. 12, the strain-induced change of the Co d -level splitting, and respective change of moment orientation from in plane (for tensile strain) to out of plane (for compressive strain) goes hand in hand with a change of the MR from negative to positive. Due to the counteracting contributions of WAL and AMR effect in the samples with compressive strain, the absolute value of the MR is much smaller than for tensile strained samples (cf. Fig. 10).

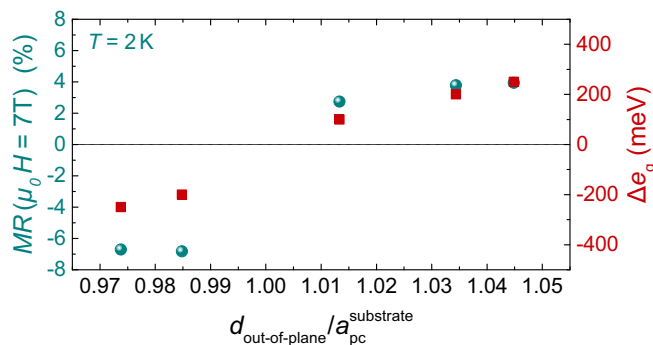


FIG. 12. Strain dependence of the MR at a magnetic field of $\mu_0 H = 7$ T at $T = 2$ K (cyan circles) in comparison to the energy difference $\Delta e_g = E_{d_{x^2-y^2}} - E_{d_{z^2}}$ (red squares) from Fig. 7(c).

IV. CONCLUSION

B-site ordered SCIO thin films have been grown on (111)_c oriented STO substrates and within a strain series also on various (pseudo)cubic (001)_{pc} oriented substrates. Our electrical transport measurements of (111)_c oriented samples with and without an air-protection layer out of STO indicated in comparison to literature results from [22] that the SCIO thin films degenerate in direct air contact. This leads us to the development of a four-step *in situ* lithographical process to investigate the temperature and magnetic field dependencies of the electrical transport properties for protected samples.

The complete strain transfer from the substrate to the thin film was checked in all cases of the (001)_{pc} strain series by reciprocal space maps around the (013)_{pc} substrate peak in combination with HAADF STEM images in [100]_{pc} direction. The, at least partial, *B*-site ordering of the SCIO thin films was proven by XRD scans in tilted geometry as well as by polarization-dependent Raman spectroscopy. HAADF STEM images in [110]_{pc} direction of selected samples reinforce these results.

The magnetic properties were investigated with SQUID magnetometry. The AFM ordering temperature $T_N \sim 43(10)$ K of the thick SCIO thin films is reduced in comparison to the bulk value ($T_N \sim 70$ K [22]). Using polarization-dependent x-ray absorption spectroscopy at the Co $L_{2,3}$ edges,

we revealed that the Co $3d$ orbital occupation strongly depends on the strain in the SCIO thin films induced by the substrates. The tensile strained SCIO thin films stabilize the occupation of the minority orbital state with x/y character, whereas the compressive strained SCIO thin films favor the occupation of the minority orbital state with z character. Together with the calculations using the well-proven configuration interaction cluster model, we were able to determine the magnetic easy-axis change due to the induced strain from the substrates, and the sign and the magnitude of the magnetic anisotropy energy of the antiferromagnetically ordered high-spin Co³⁺ ions. We presented a quantitative model including the anisotropic magnetoresistance and weak antilocalization effects to explain the opposite behavior and its magnitude of the low-temperature magnetoresistance in the tensile strained from the compressive strained SCIO thin films.

ACKNOWLEDGMENTS

The authors would like to thank S. Meir for developing the shadow mask argon ion etching method at Augsburg University and B. Meir for the support with it. We thank R. Pentcheva and P. Seiler for stimulating discussions. The work at Augsburg was supported by the Deutsche Forschungsgemeinschaft (DFG) through SPP 1666 and TRR 80. The research in Dresden was partially supported by the DFG through SFB 1143 and the study in Göttingen through SFB 1073.

-
- [1] S. Vasala and M. Karppinen, $A_2B'B''O_6$ perovskites: A review, *Prog. Solid State Chem.* **43**, 1 (2015).
- [2] A. Ohtomo, S. Chakraverty, H. Mashiko, T. Oshima, and M. Kawasaki, Spontaneous atomic ordering and magnetism in epitaxially stabilized double perovskites, *J. Mater. Res.* **28**, 689 (2013).
- [3] M. T. Anderson, K. B. Greenwood, G. A. Taylor, and K. R. Poeppelmeier, B-cation arrangements in double perovskites, *Prog. Solid State Chem.* **22**, 197 (1993).
- [4] S. Chakraverty, A. Ohtomo, D. Okuyama, M. Saito, M. Okude, R. Kumai, T. Arima, Y. Tokura, S. Tsukimoto, Y. Ikuhara, and M. Kawasaki, Ferrimagnetism and spontaneous ordering of transition metals in double perovskite $\text{La}_2\text{CrFeO}_6$ films, *Phys. Rev. B* **84**, 064436 (2011).
- [5] D. Serrate, J. M. D. Teresa, and M. R. Ibarra, Double perovskites with ferromagnetism above room temperature, *J. Phys.: Condens. Matter* **19**, 023201 (2007).
- [6] M. P. Singh, K. D. Truong, and P. Fournier, Magnetodielectric effect in double perovskite $\text{La}_2\text{CoMnO}_6$ thin films, *Appl. Phys. Lett.* **91**, 042504 (2007).
- [7] H. L. Feng, M. Arai, Y. Matsushita, Y. Tsujimoto, Y. Yuan, C. I. Sathish, J. He, M. Tanaka, and K. Yamaura, High-pressure synthesis, crystal structure and magnetic properties of double perovskite oxide $\text{Ba}_2\text{CuOsO}_6$, *J. Solid State Chem.* **217**, 9 (2014).
- [8] B. J. Kim, H. Jin, S. J. Moon, J.-Y. Kim, B.-G. Park, C. S. Leem, J. Yu, T. W. Noh, C. Kim, S.-J. Oh, J.-H. Park, V. Durairaj, G. Cao, and E. Rotenberg, Novel $J_{\text{eff}} = 1/2$ Mott State Induced by Relativistic Spin-Orbit Coupling in Sr_2IrO_4 , *Phys. Rev. Lett.* **101**, 076402 (2008).
- [9] B. J. Kim, H. Ohsumi, T. Komesu, S. Sakai, T. Morita, H. Takagi, and T. Arima, Phase-sensitive observation of a spin-orbital mott state in Sr_2IrO_4 , *Science* **323**, 1329 (2009).
- [10] Y. F. Nie, P. D. C. King, C. H. Kim, M. Uchida, H. I. Wei, B. D. Faeth, J. P. Ruf, J. P. C. Ruff, L. Xie, X. Pan, C. J. Fennie, D. G. Schlom, and K. M. Shen, Interplay of Spin-Orbit Interactions, Dimensionality, and Octahedral Rotations in Semimetallic SrIrO_3 , *Phys. Rev. Lett.* **114**, 016401 (2015).
- [11] G. Jackeli and G. Khaliullin, Mott Insulators in the Strong Spin-Orbit Coupling Limit: From Heisenberg to a Quantum Compass and Kitaev Models, *Phys. Rev. Lett.* **102**, 017205 (2009).
- [12] A. Kitaev, Anyons in an exactly solved model and beyond, *Ann. Phys.* **321**, 2 (2006).
- [13] S. M. Winter, A. A. Tsirlin, M. Daghofer, J. van den Brink, Y. Singh, P. Gegenwart, and R. Valenti, Models and materials for generalized Kitaev magnetism, *J. Phys.: Condens. Matter* **29**, 493002 (2017).
- [14] K. Momma and F. Izumi, VESTA 3 for three-dimensional visualization of crystal, volumetric and morphology data, *J. Appl. Crystallogr.* **44**, 1272 (2011).
- [15] D. Mikhailova, N. Narayanan, W. Gruner, A. Voss, A. Senyshyn, D. M. Trots, H. Fuess, and H. Ehrenberg, The role of oxygen stoichiometry on phase stability, structure, and magnetic properties of $\text{Sr}_2\text{CoIrO}_{6-\delta}$, *Inorg. Chem.* **49**, 10348 (2010).
- [16] S. Kanungo, K. Mogare, B. Yan, M. Reehuis, A. Hoser, C. Felser, and M. Jansen, Weak orbital ordering of Ir t_{2g} states in the double perovskite $\text{Sr}_2\text{CeIrO}_6$, *Phys. Rev. B* **93**, 245148 (2016).
- [17] G. Cao, A. Subedi, S. Calder, J.-Q. Yan, J. Yi, Z. Gai, L. Poudel, D. J. Singh, M. D. Lumsden, A. D. Christianson, B. C. Sales, and D. Mandrus, Magnetism and electronic structure of $\text{La}_2\text{ZnIrO}_6$

- and $\text{La}_2\text{MgIrO}_6$: Candidate $J_{\text{eff}} = 1/2$ Mott insulators, *Phys. Rev. B* **87**, 155136 (2013).
- [18] G. Cao, T. F. Qi, L. Li, J. Terzic, S. J. Yuan, L. E. DeLong, G. Murthy, and R. K. Kaul, Novel Magnetism of Ir^{5+} ($5d^4$) Ions in the Double Perovskite Sr_2YIrO_6 , *Phys. Rev. Lett.* **112**, 056402 (2014).
- [19] L. T. Corredor, G. Aslan-Cansever, M. Sturza, K. Manna, A. Maljuk, S. Gaß, T. Dey, A. U. B. Wolter, O. Kataeva, A. Zimmermann, M. Geyer, C. G. F. Blum, S. Wurmehl, and B. Büchner, Iridium double perovskite Sr_2YIrO_6 : A combined structural and specific heat study, *Phys. Rev. B* **95**, 064418 (2017).
- [20] F. Hammerath, R. Sarkar, S. Kamusella, C. Baines, H.-H. Klauss, T. Dey, A. Maljuk, S. Gaß, A. U. B. Wolter, H.-J. Grafe, S. Wurmehl, and B. Büchner, Diluted paramagnetic impurities in nonmagnetic Ba_2YIrO_6 , *Phys. Rev. B* **96**, 165108 (2017).
- [21] J.-M. Carter, V. V. Shankar, M. A. Zeb, and H.-Y. Kee, Semimetal and Topological Insulator in Perovskite Iridates, *Phys. Rev. B* **85**, 115105 (2012).
- [22] N. Narayanan, D. Mikhailova, A. Senyshyn, D. M. Trots, R. Laskowski, P. Blaha, K. Schwarz, H. Fuess, and H. Ehrenberg, Temperature and composition dependence of crystal structures and magnetic and electronic properties of the double perovskites $\text{La}_{2-x}\text{Sr}_x\text{CoIrO}_6$ ($0 \leq x \leq 2$), *Phys. Rev. B* **82**, 024403 (2010).
- [23] M. Schneider, D. Geiger, S. Esser, U. Pracht, C. Stingl, Y. Tokiwa, V. Moshnyaga, I. Sheikin, J. Mravlje, M. Scheffler, and P. Gegenwart, Low-Energy Electronic Properties of Clean CaRuO_3 : Elusive Landau Quasiparticles, *Phys. Rev. Lett.* **112**, 206403 (2014).
- [24] R. Egoavil, S. Hühn, M. Jungbauer, N. Gauquelin, A. Béché, G. Van Tendeloo, J. Verbeeck, and V. Moshnyaga, Phase problem in the B-site ordering of $\text{La}_2\text{CoMnO}_6$: Impact on structure and magnetism, *Nanoscale* **7**, 9835 (2015).
- [25] M. Jungbauer, S. Hühn, M. Michelmann, E. Goering, and V. Moshnyaga, Exchange bias in $\text{La}_{0.7}\text{Sr}_{0.3}\text{MnO}_3/\text{SrMnO}_3/\text{La}_{0.7}\text{Sr}_{0.3}\text{MnO}_3$ trilayers, *J. Appl. Phys.* **113**, 17D709 (2013).
- [26] S. Macke, S. Brück, P. Audehm, M. Harlander, and E. Goering, ReMagX: X-ray Magnetic Reflectivity Tool, 2009, available at <http://www.mf.mpg.de/remagx.html>.
- [27] See Supplemental Material at <http://link.aps.org/supplemental/10.1103/PhysRevB.97.205121> for details concerning the *in situ* lithographical process, additional structural information, the foreign phase determination, details of the zero-field transport properties as well as the magnetoresistance model and additional XAS spectra. See Refs. [46–58].
- [28] M. N. Iliev, M. V. Abrashev, A. P. Litvinchuk, V. G. Hadjiev, H. Guo, and A. Gupta, Raman spectroscopy of ordered double perovskite $\text{La}_2\text{CoMnO}_6$ thin films, *Phys. Rev. B* **75**, 104118 (2007).
- [29] K. D. Truong, J. Laverdière, M. P. Singh, S. Jandl, and P. Fournier, Impact of Co/Mn cation ordering on phonon anomalies in $\text{La}_2\text{CoMnO}_6$ double perovskites: Raman spectroscopy, *Phys. Rev. B* **76**, 132413 (2007).
- [30] C. Meyer, S. Hühn, M. Jungbauer, S. Merten, B. Damaschke, K. Samwer, and V. Moshnyaga, Tip-enhanced Raman spectroscopy (TERS) on double perovskite $\text{La}_2\text{CoMnO}_6$ thin films: Field enhancement and depolarization effects, *J. Raman Spectrosc.* **48**, 46 (2017).
- [31] D. Kumar and D. Kaur, Structural and magnetic properties of $\text{La}_2\text{NiMnO}_6$ thin films on LaAlO_3 substrate with varying thickness, *J. Alloys Compd.* **554**, 277 (2013).
- [32] A. J. Hauser, R. E. A. Williams, R. A. Ricciardo, A. Genc, M. Dixit, J. M. Lucy, P. M. Woodward, H. L. Fraser, and F. Yang, Unlocking the potential of half-metallic $\text{Sr}_2\text{FeMoO}_6$ films through controlled stoichiometry and double-perovskite ordering, *Phys. Rev. B* **83**, 014407 (2011).
- [33] S. Esser, Verspannungsinduzierte Änderungen der elektronischen Eigenschaften von $\text{Sr}_2\text{CoIrO}_6$ Dünnschichten, Ph.D. thesis, University of Augsburg, 2018.
- [34] A. Belenchuk, O. Shapoval, V. Roddatis, V. Bruchmann-Bamberg, K. Samwer, and V. Moshnyaga, Ruddlesden-Popper interface in correlated manganite heterostructures induces magnetic decoupling and dead layer reduction, *Appl. Phys. Lett.* **109**, 232405 (2016).
- [35] M. W. Haverkort, S. I. Csiszar, Z. Hu, S. Altieri, A. Tanaka, H. H. Hsieh, H.-J. Lin, C. T. Chen, T. Hibma, and L. H. Tjeng, Magnetic versus crystal-field linear dichroism in NiO thin films, *Phys. Rev. B* **69**, 020408(R) (2004).
- [36] S. I. Csiszar, M. W. Haverkort, Z. Hu, A. Tanaka, H. H. Hsieh, H.-J. Lin, C. T. Chen, T. Hibma, and L. H. Tjeng, Controlling Orbital Moment and Spin Orientation in CoO Layers by Strain, *Phys. Rev. Lett.* **95**, 187205 (2005).
- [37] C.-Y. Kuo, Z. Hu, J. C. Yang, S.-C. Liao, Y. L. Huang, R. K. Vasudevan, M. B. Okatan, S. Jesse, S. V. Kalinin, L. Li, H. J. Liu, C.-H. Lai, T. W. Pi, S. Agrestini, K. Chen, P. Ohresser, A. Tanaka, L. H. Tjeng, and Y. H. Chu, Single-domain multiferroic BiFeO_3 films, *Nat. Commun.* **7**, 12712 (2016).
- [38] Z. Hu, H. Wu, M. W. Haverkort, H. H. Hsieh, H.-J. Lin, T. Lorenz, J. Baier, A. Reichl, I. Bonn, C. Felser, A. Tanaka, C. T. Chen, and L. H. Tjeng, Different Look at the Spin State of Co^{3+} Ions in a CoO_5 Pyramidal Coordination, *Phys. Rev. Lett.* **92**, 207402 (2004).
- [39] C. F. Chang, Z. Hu, H. Wu, T. Burnus, N. Hollmann, M. Benomar, T. Lorenz, A. Tanaka, H.-J. Lin, H. H. Hsieh, C. T. Chen, and L. H. Tjeng, Spin Blockade, Orbital Occupation, and Charge Ordering in $\text{La}_{1.5}\text{Sr}_{0.5}\text{CoO}_4$, *Phys. Rev. Lett.* **102**, 116401 (2009).
- [40] S. Agrestini, C.-Y. Kuo, D. Mikhailova, K. Chen, P. Ohresser, T. W. Pi, H. Guo, A. C. Komarek, A. Tanaka, Z. Hu, and L. H. Tjeng, Intricacies of the Co^{3+} spin state in $\text{Sr}_2\text{Co}_{0.5}\text{Ir}_{0.5}\text{O}_4$: An x-ray absorption and magnetic circular dichroism study, *Phys. Rev. B* **95**, 245131 (2017).
- [41] F. M. F. de Groot, X-ray absorption and dichroism of transition metals and their compounds, *J. Electron Spectrosc. Relat. Phenom.* **67**, 529 (1994).
- [42] A. Tanaka and T. Jo, Resonant $3d$, $3p$ and $3s$ photoemission in transition metal oxides predicted at $2p$ threshold, *J. Phys. Soc. Jpn.* **63**, 2788 (1994).
- [43] R. Galceran, L. Lopez-Mir, B. Bozzo, J. Cisneros-Fernandez, J. Santiso, L. Balcells, C. Frontera, and B. Martinez, Strain-induced perpendicular magnetic anisotropy in $\text{La}_2\text{CoMnO}_{6-\epsilon}$ thin films and its dependence on film thickness, *Phys. Rev. B* **93**, 144417 (2016).
- [44] L. Lopez-Mir, R. Galceran, J. Herrero-Martin, B. Bozzo, J. Cisneros-Fernandez, E. V. Pannunzio Miner, A. Pomar,

- L. Balcells, B. Martinez, and C. Frontera, Magnetic anisotropy and valence states in $\text{La}_2\text{Co}_{1-x}\text{Mn}_{1+x}\text{O}_6$ ($x \approx 0.23$) thin films studied by x-ray absorption spectroscopy techniques, *Phys. Rev. B* **95**, 224434 (2017).
- [45] P. D. Dresselhaus, C. M. A. Papavassiliou, R. G. Wheeler, and R. N. Sacks, Observation of Spin Precession in GaAs inversion Layers Using Antilocalization, *Phys. Rev. Lett.* **68**, 106 (1992).
- [46] R. R. Birss, *Symmetry and Magnetism, Band 863* (North-Holland, Amsterdam, 1964).
- [47] P. K. Muduli, K.-J. Friedland, J. Herfort, H.-P. Schönherr, and K. H. Ploog, Antisymmetric contribution to the planar Hall effect of Fe_3Si films grown on GaAs(113)A substrates, *Phys. Rev. B* **72**, 104430 (2005).
- [48] P. Hartel, H. Rose, and C. Dinges, Conditions and reasons for incoherent imaging in STEM, *Ultramicroscopy* **63**, 93 (1996).
- [49] X. X. Wang, J. J. Li, Y. G. Shi, Y. Tsujimoto, Y. F. Guo, S. B. Zhang, Y. Matsushita, M. Tanaka, Y. Katsuya, K. Kobayashi, K. Yamaura, and E. Takayama-Muromachi, Structure and magnetism of the postlayered perovskite $\text{Sr}_3\text{Co}_2\text{O}_6$: A possible frustrated spin-chain material, *Phys. Rev. B* **83**, 100410 (2011).
- [50] N. F. Mott, Conduction in non-crystalline materials: III. Localized states in a pseudogap and near extremities of conduction and valence bands, *Philos. Mag.* **19**, 835 (1969).
- [51] G. Bergmann, Weak localization in thin films: A time-of-flight experiment with conduction electrons, *Phys. Rep.* **107**, 1 (1984).
- [52] P. W. Anderson, E. Abrahams, and T. V. Ramakrishnan, Possible Explanation of Nonlinear Conductivity in Thin-Film Metal Wires, *Phys. Rev. Lett.* **43**, 718 (1979).
- [53] L. Fruchter, G. Collin, D. Colson, and V. Brouet, Sr_2IrO_4 magnetic phase diagram from resistivity, *Eur. Phys. J. B* **88**, 141 (2015).
- [54] T. Wu, S. B. Ogale, J. E. Garrison, B. Nagaraj, A. Biswas, Z. Chen, R. L. Greene, R. Ramesh, T. Venkatesan, and A. J. Millis, Electroresistance and Electronic Phase Separation in Mixed-Valent Manganites, *Phys. Rev. Lett.* **86**, 5998 (2001).
- [55] R. Ghosh, D. Basak, and S. Fujihara, Effect of substrate-induced strain on the structural, electrical, and optical properties of polycrystalline ZnO thin films, *J. Appl. Phys.* **96**, 2689 (2004).
- [56] W. Limmer, J. Daeubler, L. Dreher, M. Glunk, W. Schoch, S. Schwaiger, and R. Sauer, Advanced resistivity model for arbitrary magnetization orientation applied to a series of compressive- to tensile-strained (Ga, Mn)As layers, *Phys. Rev. B* **77**, 205210 (2008).
- [57] T. McGuire and R. L. Potter, Anisotropic magnetoresistance in ferromagnetic 3d alloys, *IEEE Trans. Magn.* **11**, 1018 (1975).
- [58] O. Bilani-Zeneli, A. D. Rata, A. Herklotz, O. Mieth, L. M. Eng, L. Schultz, M. D. Biegalski, H. M. Christen, and K. Dörr, SrTiO_3 on piezoelectric PMN-PT(001) for application of variable strain, *J. Appl. Phys.* **104**, 054108 (2008).